Title
MOLECULAR BEAM SOURCES FABRICATED FROM MULTICHANNEL ARRAYS. PART II - EFFECT OF SOURCE SIZE AND ALIGNMENT

Author
Olander, Donald R.

Publication Date
1969

Submitted to the J. of Applied Physics

UCRL-18700
Preprint

ey. 2

MOLECULAR BEAM SOURCES FABRICATED FROM MULTICHANNEL ARRAYS
Part II - Effect of Source Size and Alignment

Donald R. Olander

January 1969

AEC Contract No. W-7405-eng-48

LAWRENCE RADIATION LABORATORY
UNIVERSITY of CALIFORNIA BERKELEY

ey. 2

UCRL-18700

DISCLAIMER

MOLECULAR BEAM SOURCES FABRICATED FROM MULTICHANNEL ARRAYS

Part II - Effect of Source Size and Alignment

Donald R. Olander

Inorganic Materials Research Division, Lawrence Radiation Laboratory,
Department of Nuclear Engineering, College of Engineering,
University of California, Berkeley, California

ABSTRACT

The effect of the gross diameter of a molecular beam source and its alignment in the system upon source efficiency have been investigated analytically. If the diameter of the source approaches that of the collimating orifice used to form the molecular beam, the efficiency may be reduced by 50% or more. Reasonable displacement and tilt misalignments can be tolerated before source efficiency is substantially reduced. The effects of size and misalignment are more critical for multichannel sources with highly peaked angular distributions than for cosine sources.

17859

INTRODUCTION

The prime purpose of a molecular beam source is to generate the largest possible centerline intensity at a specified total flow rate. Part I demonstrated that multichannel sources are capable of producing significantly stronger beams than thin-walled orifices. Here the effects of the size of the source and imperfect alignment of the source tube upon the utilization of the very favorable angular distributions in practical systems are investigated.

The strength of the usable molecular beam depends upon the geometry of the system in which the source is placed as well as on the angular distribution from the source. The three essential elements of the geometry are: (1) the source; (2) the collimator; and (3) the target.

Since multichannel sources require packing together of a large number of small bore tubes, the overall radius of the tube bundle is generally too large to be adequately approximated as a point emitter. The gross radius of the source is denoted by r_s.

In nearly all molecular beam systems, the central portion of the efflux from the source is skimmed off by a collimator downstream of the source to form the molecular beam. The collimator radius is r_1 and its distance from the source is d. The target is located at a distance d_T downstream of the source. These dimensions are depicted in Fig. 1, which represents a typical molecular beam apparatus.*

---

* The insertion of a buffer chamber between the two chambers shown in Fig. 1 does not alter the calculations here. The primary purpose of a buffer chamber is to permit differential pumping, and it does not contribute to beam formation.

As in Part I, beam intensities are referenced to the strength of the beam from an ideal thin-walled orifice emitting at the same total rate and subject to the same geometrical restraints except that of source size. The reference cosine emitter is assumed to be a true point source ($r_s \to 0$). These reference conditions have been chosen because they represent the method by which molecular beam systems are currently designed. The results of the present analysis can be used simply as multiplicative correction factors to account for the effects of source size, non-cosine emission, and possible misalignments in assembly.

By referring the actual source to the point cosine standard, only three characteristic dimensions are needed for the computations. These have been chosen as the ratios:

$$Q = r_s/r_1 \tag{1}$$

$$R = r_1/d \tag{2}$$

$$T = d/d_T \tag{3}$$

In many beam systems, the source and collimator diameters are both approximately equal, and the ratio Q is of the order of unity. The axial distances d and d_T are generally much larger than either r_1 or r_s, and the ratio R is very small (~ 0.01). The ratio T is typically between 0.2 and 0.9.

The radius of the beam impinging on the target is generally designed to be that of a beam from a true point source, or

$$r_T = r_1\left(\frac{d_T}{d}\right) \tag{4}$$

In the case of a true point source, all beam molecules striking the target are contained in a circle of radius r_T. For a source of non-zero dimension, a penumbra is created, and a portion of the beam strikes the

target at radial distances greater than r_T. In many systems, the penumbra may be purposely eliminated by insertion of a second collimating aperture between the first orifice and the target. In other experiments, the nature of the target itself may render the penumbral portion of the beam unusable. For the purposes of this computation, the molecules in the penumbra are disregarded and only the flux within radius r_T at the target is calculated.

Given a source of gross radius r_s, the entire active area of which emits molecules in a specified angular distribution pattern and with a hemispherical strength of S molecules/cm^2-sec, the following two quantities can be computed:

(a) The beam intensity as a function of position on the target.

(b) The rate at which molecules strike the usable portion of the target (i.e., the integral of (a) up to a target radius of r_T).

The centerline beam intensity from a point source with a cosine distribution is

$$I^*(0) = S\left(\frac{r_s}{d_T}\right)^2, \ \frac{\text{molecules}}{\text{cm}^2\text{-sec}} \qquad (5)$$

If, in addition, the geometry is such that the radius of the collimating aperture is much smaller than the source-to-collimator distance, the total impingement rate on the target from a point cosine emmitter is:

$$N^* = \pi r_s^2 \, S\left(\frac{r_1}{d}\right)^2, \ \frac{\text{molecules}}{\text{sec}} \qquad (6)$$

For the actual source, the ratios $[I(\rho_T, \phi_T)/I^*(0)]$ and N/N^* are computed, where ρ_T and ϕ_T denote the radial and azimuthal coordinates of an off-center location on the target.

These ratios can be interpreted in terms of peaking factors introduced in Part I. The ratio I/I^* is the peaking factor as a function of

location on the target. If N and N* are both divided by πr_T^2, the ratio N/N* can be viewed as the average peaking factor. Thus:

$$\chi(\rho_T,\phi_T) = I(\rho_T,\phi_T)/I^*(0) \tag{7}$$

$$\bar{\chi} = N/N^* \tag{8}$$

The peaking factor discussed in Part I is $\chi(0)$. The usable quantity in a real experiment, however, is $\bar{\chi}$.

$\chi(\rho_T,\phi_T)$ and $\bar{\chi}$ can be expressed in terms of the length ratios Q, R, and T and similar parameters denoting the extent of misalignment of the source tube with respect to the axis defined by the normal to the collimating aperture.

THE EFFECT OF SOURCE SIZE

The effect of source radii greater than zero is to reduce the average peaking factor $\overline{X}$ below the maximum value $X(0)$. In this computation, alignment of the source tube is assumed to be perfect, and the effect of Q on the peaking factor is determined for a cosine emitter and a typical highly peaked multichannel source.

The diagram for performing the calculations is shown in Fig. 2. The rate of emission of molecules from an element of area dA_s on the source disk into a unit solid angle at polar angle θ is $SJ(\theta)dA_s$, where $J(\theta)$ is the angular distribution function of the source, normalized so that:

$$2\pi \int_0^1 J(\theta) d(\cos\theta) = 1 \qquad (9)$$

The solid angle subtended by an element of target area dA_T seen from dA_s is $\cos\theta dA_T/y^2$. The product of these two factors is the rate at which molecules from dA_s strike dA_T. From Fig. 2, it can be seen that:

$$\cos\theta = d_T/y$$

$$y^2 = d_T^2 + \rho_T^2 + \rho_s^2 - 2\rho_s\rho_T\cos\phi_s$$

Using these relations and integrating over the portion of the source disk which can see the spot on the target at a radial location ρ_T yields the beam intensity:

$$I(\rho_T) = 2S \int_{\phi_s\,min}^{\pi} d\phi_s \int_{\rho_{s1}}^{\rho_{s2}} \frac{d_T\, J(\theta)}{[d_T^2 + \rho_T^2 + \rho_s^2 - 2\rho_s\rho_T \cos\phi_s]^{3/2}} \rho_s d\rho_s \qquad (10)$$

Because of azimuthal symmetry, the beam intensity is not a function of ϕ_T. Using the dimensionless variables

$$U = \rho_s/r_1 \qquad (11)$$

$$V = \rho_T/r_1 \qquad (12)$$

$$G_1 = \rho_{s1}/r_1 \tag{13}$$

$$G_2 = \rho_{s2}/r_1 \tag{14}$$

and dividing by $I^*(0)$ yields:

$$\chi(V) = \frac{2}{Q^2(RT)^3}\int_{\phi_s\,min}^{\pi} d\phi_s \int_{G_1}^{G_2} \frac{J(\theta)\,UdU}{\left[(RT)^{-2} + V^2 + U^2 - 2UV\cos\phi_s\right]^{3/2}} \tag{15}$$

For a cosine emitter ($J(\theta) = \cos\theta/\pi$), the U integral can be performed analytically.

The limits on the integrals in this equation require some examination of the geometry of the system. For a given point ρ_T (or V) on the target, only a part of the source disk may be capable of contributing to the current at a particular location on the target. This region is the common area of overlap between the source disk of radius r_s (or Q) and the figure resulting from projection of the collimating orifice on the source plane from the location ρ_T on the target. It can be shown that this image of the collimator is a circle the radius of which is independent of ρ_T and equal to $(\frac{d_T}{d_T-d})r_1$. The center of this circle is a distance $(\frac{d}{d_T-d})\rho_T$ from the center of the source disk. Made dimensionless with respect to r_1, the radius of the collimator image on the source plane is:

$$W_i = \frac{1}{1 - T} \tag{16}$$

and the distance from the center of the source disk is:

$$W = \frac{TV}{1 - T} \tag{17}$$

The integration limits in Eq. (15) depend on whether W_i is larger or smaller than W. The regions of integration on the source plane for these two cases are shaded in Fig. (3). The limits of integration are:

(a) (the umbra) $0 \leq V \leq 1/T$:

$$\phi_s^{min} = 0 \tag{18}$$

$$G_1 = 0 \tag{19}$$

$$G_2 = (W \cos \phi_s)\left[-1 \pm \sqrt{1 + \frac{W_i^2 - W^2}{(W \cos \phi_s)^2}}\right] \text{ or } Q, \text{ whichever is smaller} \tag{20}$$

The positive root applies for $0 \leq \phi_s \leq \pi/2$ and the negative root for $\pi/2 \leq \phi_s \leq \pi$.

(b) (the penumbra) $1/T \leq V \leq 1/T + Q$

The upper limit on V corresponds to the point of tangency of the two circles in Fig. (3b). At this position on the target, the source disk has just disappeared from view:

$$\phi_s^{min} = \cos^{-1}\left[\frac{W_i^2 - W^2 - Q^2}{2WQ}\right] \tag{21}$$

$$G_1 = (W \cos \phi_s)\left[-1 + \sqrt{\frac{W_i^2 - W^2}{(W \cos \phi_s)^2} + 1}\right] \tag{22}$$

$$G_2 = Q \tag{23}$$

The average peaking factor is obtained by integration of Eq. (15) over the umbra:

$$\bar{\chi} = 2T^2 \int_0^{1/T} \chi(V)\, V dV \tag{24}$$

AVERAGE PEAKING FACTOR FOR COSINE SOURCES

In a practical molecular beam system, the radii of the source disk, the collimator, and the beam spot on the target are all much smaller than either the source-to-collimator or the source-to-target distances. This means that the cosine of the emission angle θ can be approximated by unity. The bracketed term in Eq. (15) reduces to $(RT)^{-3}$, which is cancelled by the same term outside of the integral. Consequently, the beam intensity and flux ratios are independent of R, and are functions of the collimator radius only through the parameter Q. Fig. (4) shows the variation of $\overline{X}$ with Q for a number of values of T. This plot is valid for all R between 0.005 and 0.1. The lower curve represents the limit as $T \to 0$. The loss of point source character is greatest for large Q and small T.

In designing a molecular beam system, it is desirable to maintain the source radius r_s (or the dimensionless parameter Q) as small as possible. This will insure that $\overline{X}$ is close to unity and that the source can be adequately approximated by a point. The efficiency of a particular source design utilizing a cosine emitter can be determined directly from Fig. 4.

The computations for a non-cosine emitter are straight-forward, but the U integral of Eq. (15) can no longer be performed analytically, nor can the cosine of the emission angle be approximated by unity. The average peaking factor is a function of the angular distribution $J(\theta)$ which characterizes the source and the three ratios Q,R, and T which characterize the system geometry.

VARIATION OF THE BEAM INTENSITY OVER THE TARGET

The intensity $I(\rho_T)$ or the peaking factor $X(V)$ represents the strength of the molecular beam at various radial positions on the target. Results of the beam intensity profile calculations are shown in Fig. 5 for R and T values of a typical molecular beam apparatus and two Q values, zero (representing a true point source) and unity (a typical value for a practical source).

For a point cosine source, the beam intensity remains constant up to the edge of the umbra, and thereafter is zero. If this same source is spread over a finite area (dashed Q = 1 curve), the beam intensity begins to drop off at approximately 40% of the usable target radius and there is a substantial tail in the penumbra. The average peaking factor, or the ratio of the usable beam for the finite source to that from the point source, is 0.734. The loss in average beam strength due to the non-zero source dimension is not severe for the cosine emitter.

The same calculations were repeated for the highly peaked distribution of Fig. 16 of Part I. The angular distribution from this source was approximated analytically by

$$J(\theta) = \begin{cases} 4.01\, e^{-15.6\theta}, & \theta < 0.026 \\ 3.33\, e^{-8.5\theta}, & 0.026 \leq \theta \leq 0.14 \\ 1.79\, e^{-4.0\theta}, & \theta > 0.14 \end{cases} \qquad (25)$$

The central peaking factor $X(0)$ is 12.6 for this source. The same geometry (R and T) was used in the calculations. The beam intensity profiles for Q = 0 and Q = 1 are also shown in Fig. 5. Even for the point source, the beam intensity drops by nearly half as the outer edge of the umbra is

approached. By contrast, the point cosine source in the same geometry yielded a uniform beam intensity in the umbra. In the case of very peaked sources, however, the small polar angle at the outer portion of the umbra (0.044 radians in this example) is sufficient to cause a substantial drop in the beam intensity. This effect can be seen directly from the angular distribution of Fig. 16 of Part I [Eq. (25)]. The centerline intensity of 12.6 in Fig. 5 correspond to the peak of this distribution.

The loss in average beam strength is even more severe if the highly peaked source is spread over a finite area (solid Q = 1 curve of Fig. 5). In this case even the centerline intensity $\chi(0)$ does not achieve the maximum value of 12.6; the outer portion of the source disk must emit at a polar angle of r_s/r_T = QRT = 0.016 off the individual channel axis in order to contribute to the centerline flux. Even this small angle is enough to cause the beam intensity to decrease 20% below its value along the axis of the individual channels. The average peaking factor is 6.10.

EFFECT OF SOURCE MISALIGNMENT

Because of the extremely peaked character of the angular distributions such as the one shown in Fig. 16 of Part I, the design of a molecular beam system utilizing such a source must consider the effect of imperfect alignment of the source tube with respect to the axis through the collimator. Fig. 6 illustrates the two possible types of misalignment.

(1) Displacement - the center of the source disk is displaced from the point of intersection of the collimator axis and the source plane by a distance ε, or in dimensionless terms,

$$E = \varepsilon / r_1 \tag{26}$$

(2) Tilt - the plane containing the source disk is tilted by an angle α with respect to the collimator axis.

For perfect alignment, both E and α are zero.

In place of Eq. (15), the local beam intensity on the target is given by:

$$\chi(V,\phi_T) = \frac{1}{Q^2(RT)^2}\int_0^{2\pi} d\phi_s \int_{G_1}^{G_2} J(\theta)\,\frac{\cos\delta}{Y^2}\,U\,dU \tag{27}$$

where Y is the dimensionless distance (with respect to the collimator radius) between a point on the source disk at ρ_s,ϕ_s and a location on the target at ρ_T,ϕ_T:

$$Y^2 = \mathcal{D}_1^2 - (\mathcal{D}_2 - \mathcal{D}_1)^2 + V'^2 + U^2 - 2UV'\cos(\phi_s - \beta) \tag{28}$$

where U and ϕ_s are, as before, the coordinates of the source plane, and

$$V' = V\left[\sin^2\phi_T + \left(\frac{\cos\phi_T}{\cos\alpha}\right)^2\right]^{1/2} \tag{29}$$

$$\beta = \tan^{-1}\left[\cos\alpha\,\tan\phi_T\right] \tag{30}$$

$$\mathcal{D}_1 = (RT)^{-1} + U\cos\phi_s\,\sin\alpha \tag{31}$$

$$\mathcal{O}_2 = (RT)^{-1} + V \cos\phi_T \tan\alpha \tag{32}$$

δ is the angle between the normal to the target plane and the ray joining a spot on the source disk with the particular target location

$$\cos\delta = \mathcal{O}_1/N \tag{33}$$

The emission angle θ is given by:

$$\cos\theta = \frac{\cos\alpha}{2Y\,\mathcal{O}_1}\left[Y^2 + \left(\frac{\mathcal{O}_1}{\cos\alpha}\right)^2 - X^2\right] \tag{34}$$

where

$$X^2 = \left[\mathcal{O}_1 \tan\alpha - V\cos\phi_T + U\cos\phi_s\cos\alpha\right]^2 + \left[V\sin\phi_T - U\sin\phi_s\right]^2 \tag{35}$$

If $\alpha = 0$, Eq. (27) reduces to Eq. (15).

The limits of integration are determined by the region of overlap between the source disk and the image of the collimator projected on the source plane from a point on the target plane. The image curve is no longer a circle of fixed radius, as it was for an untilted source plane. Rather, it is obtained by determining the intersection of the source plane with the surface represented by the locus of lines in Fig. 6 emanating from the target location and passing through the circle described by the collimator orifice periphery. The equation of the image curve in terms of the source plane coordinates U and ϕ_s is:

$$\left[U\cos\phi_s\cos\alpha + \left(\frac{TV}{1-T}\right)\cos\phi_T(RU\cos\phi_s\sin\alpha + 1)\right]^2 + \left[U\sin\phi_s + \left(\frac{TV}{1-T}\right)\sin\phi_T(RU\cos\phi_s\sin\alpha + 1)\right]^2 = \left[1 + \left(\frac{T}{1-T}\right)(RU\cos\phi_s\sin\alpha + 1)\right]^2 \tag{36}$$

which reduces to a circle of radius $1/(1-T)$ displaced from the origin by a distance $TV/(1-T)$ when $\alpha = 0$.

The equation for the source disk is

$$(U \cos\phi_s + E)^2 + (V \sin\phi_s)^2 = Q^2 \qquad (37)$$

where E is the extent of displacement, given by Eq. (26).

It proved too cumbersome to express the integration limits G_1, G_2, and ϕ_s^{min} analytically for the case of the two curves represented by Eqs. (36) and (37). Instead, a procedure readily adapted to machine computation was utilized. For each angle on the source plane ϕ_s, the roots of Eqs. (36) and (37) were determined. If the roots of either one of these equations were imaginary, the line through the coordinate origin on the source plane at the selected ϕ_s did not intersect that curve. The U integral at this value of ϕ_s was set equal to zero. This method is equivalent to analytical determination of the limits on the ϕ_s integral of Eq. (27). At source plane angles for which the roots of both equations were real, a series of sign and relative magnitude checks was used to determine whether there was a true segment of overlap in the chosen direction. The limits of the U integral in Eq. (27) were selected from the four possibilities (two roots from each curve) and the integration performed numerically.

Since the beam intensity on the target, or $X(V,\phi_T)$, depends upon five geometrical parameters (Q,R,T,E, and α) and the angular distribution function characterizing the particular source $[J(\theta)]$, the effect of all possible parameter combinations could not be explored. Instead, the geometrical parameters of the molecular beam apparatus were fixed and the effect of the two types of misalignment were investigated separately for a cosine source and the multichannel source characterized by the angular distribution of Eq. (25). The geometrical parameters were those

previously used in the calculation of the effect of source size (R = 0.044 and T = 0.37). The source size parameter, Q, was fixed at unity. The beam intensity profiles for perfect alignment of the two sources are shown in Fig. 5. The average peaking factors for the Q = 1 source size are 0.734 for the cosine emitter and 6.10 for the multichannel source.

A polar diagram of the beam intensity contours for the perfectly aligned multichannel source is shown in Fig. 7. The same source misaligned by one collimator radius displacement of the source tube axis from the collimator axis generates the contours shown in Fig. 8. The effect of a tilt misalignment of $\sim 6°$ from the collimator axis is shown in Fig. 9. For both types of misalignment, the peak intensity is significantly less than that of the perfectly aligned source and the location of the maximum has moved from the target center in the expected direction.

Average peaking factors are obtained by integration of $\chi(V,\phi_T)$ over the region contained within the dashed lines of Figs. 7 - 9, which delineate the boundary of the usable target area. The effect of displacement misalignment on the average peaking factor shown in Fig. 10 is not as disastrous as might have been expected from the sharpness of the angular distribution (Fig. 16 of Part I). The efficiency drops by only 28% for a displacement of one collimator radius (for a typical system, this represents about 1/2 mm). However, if the misalignment is greater than 2 collimator radii, the overall efficiency of the multichannel source is no better than that of a well-aligned point cosine source.

The effect of tilt misalignment on the same sources is shown in Fig. 11. Here, the loss in average beam intensity on the target is much more severe for the multichannel source than for a cosine source.

However, the decrease in $\bar{\chi}$ with α is not as rapid as the decrease of the angular distribution function with emission angle, which intuitively would seem a reasonable first approximation. The reason for the relatively gradual loss in peaking factor with tilt angle lies in the geometry of the source-target interaction. As the source plane is tilted from the normal to the collimator axis, only molecules emitted at an angle of α contribute to the beam. However, the weaker flux from the individual channels is partially compensated by the larger fraction of the source disk which, because of the foreshortening due to the tilt, can be seen by the target.

The effect of simultaneous tilt and displacement was explored briefly. In particular, it was of interest to determine whether the fractional decrease in peaking factor due to each misalignment considered separately could be multiplied together to predict the general misalignment, or whether the relation

$$\bar{\chi}\,(E,\alpha) \sim \bar{\chi}\,(E,0)\;\bar{\chi}\,(0,\alpha)/\;\bar{\chi}\,(0,0) \qquad (38)$$

could be used as a first approximation. $\bar{\chi}(1,0.1)$ calculated by the above formula was 20% smaller than the result obtained from the full computation. At least for the geometry chosen here, Eq. (38) provides a conservative estimate of the combined misalignment effects.

As discussed in connection with Fig. 4, the average peaking factors for a cosine emitter are essentially independent of the parameter R because of the insensitivity of a cosine distribution to polar angle in the neighborhood of the normal. Sources with angular distributions like Eq. (25), on the other hand, are extremely sensitive to small changes in emission angle off the normal. These distributions exhibit cusps at $\theta = 0$

(see Fig. 16 of Part I) whereas a cosine distribution is nearly flat at $\theta = 0$. A modest effect of the parameter R on the average peaking factor was computed for the multichannel source used as an example in this study. Decreasing R by a factor of two (from a value of 0.044) produced a decrease of 10% in $\bar{\chi}$.

CONCLUSIONS

The computations presented here suggest that even highly peaked multichannel sources are not overly susceptible to loss of efficiency due to tilt or displacement misalignments. If the tilt relative to the collimator axis can be kept less than ~1° and the displacement less than ~ 1/2 of a collimator radius, the single biggest loss in efficiency is due to the size of the source disk rather than imperfect alignment. Tolerances of this order appear to be readily attainable with good machining and assembly techniques and vacuum components of reasonable quality.

For the typical system geometry and source characteristics studied here, the price of bundling individual channels each with a centerline peaking factors of 12.6 into a source of overall diameter equal to that of the collimating orifice is paid for in the average peaking factor, which is 6.1. The great improvement in directivity of the individual channels over a cosine emitter has been reduced by 50% simply by the unavoidable process of assembling them into a source of non-zero diameter. There are several methods of avoiding this degradation of efficiency: The first is to pack the individual channels closer together. This is generally not practical, since sources of the type which give distributions shown in Fig. 16 of Part I are already 50% transparent. The second is to make the collimating aperature larger, which reduces the value of Q. However, there are generally limitations on the maximum size of the beam spot on the target which can be tolerated, and the collimator radius is usually fixed by these considerations. The third is to increase T(or the ratio d/d_T),which for a fixed Q increases the average peaking factor

(see Fig. 4 for this effect in cosine sources). Practically, a minimum space between the collimator and the target is needed for a variety of reasons (detector, beam flag, or modulator may be inserted here, the target may be operated at high temperatures, etc.). For a fixed difference between d_T and d, the ratio d/d_T can be increased only by making d_T larger. This remedy, however, decreases the total beam intensity by the $1/(\text{distance})^2$ effect, and is the least desirable approach.

Consequently, it appears that practical molecular beam sources fabricated from multichannel arrays cannot attain their maximum single-channel peaking factors. When operated at high Knudsen numbers (or low reduced source pressures), they still can provide a 5-6 fold improvement in average intensity over a cosine emitter at the same leak rate, but probably never will realize the order of magnitude increase which was originally anticipated.

Acknowledgement - This work was supported by the United States Atomic Energy Commission.

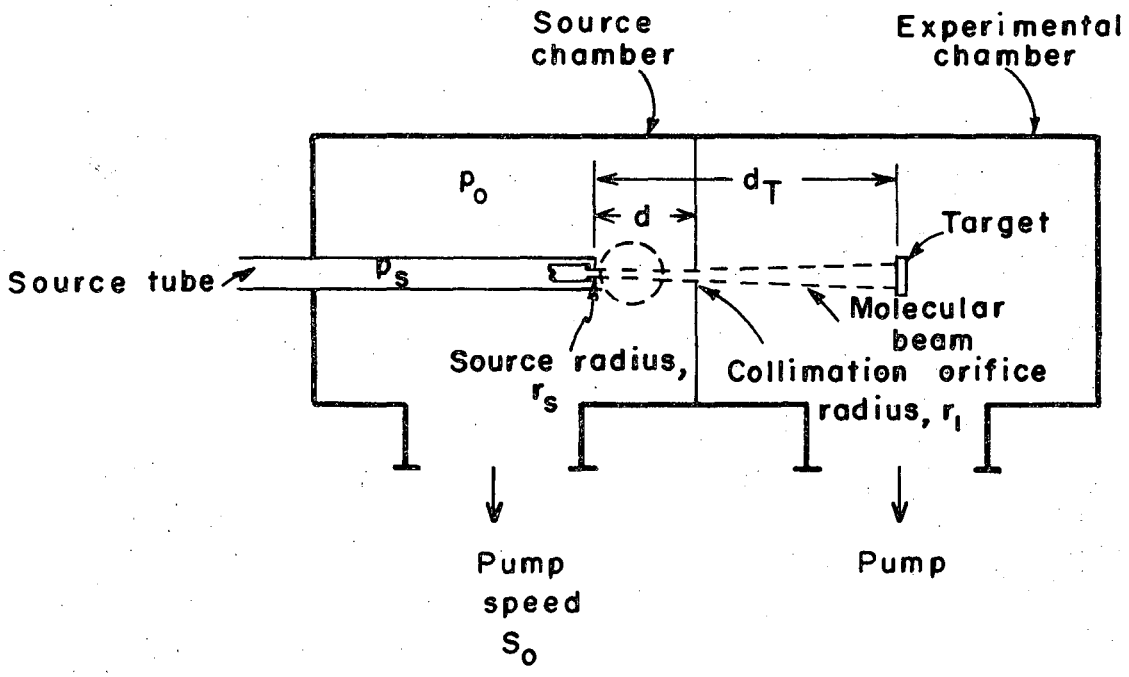

Fig. 1 Schematic of typical molecular beam apparatus.

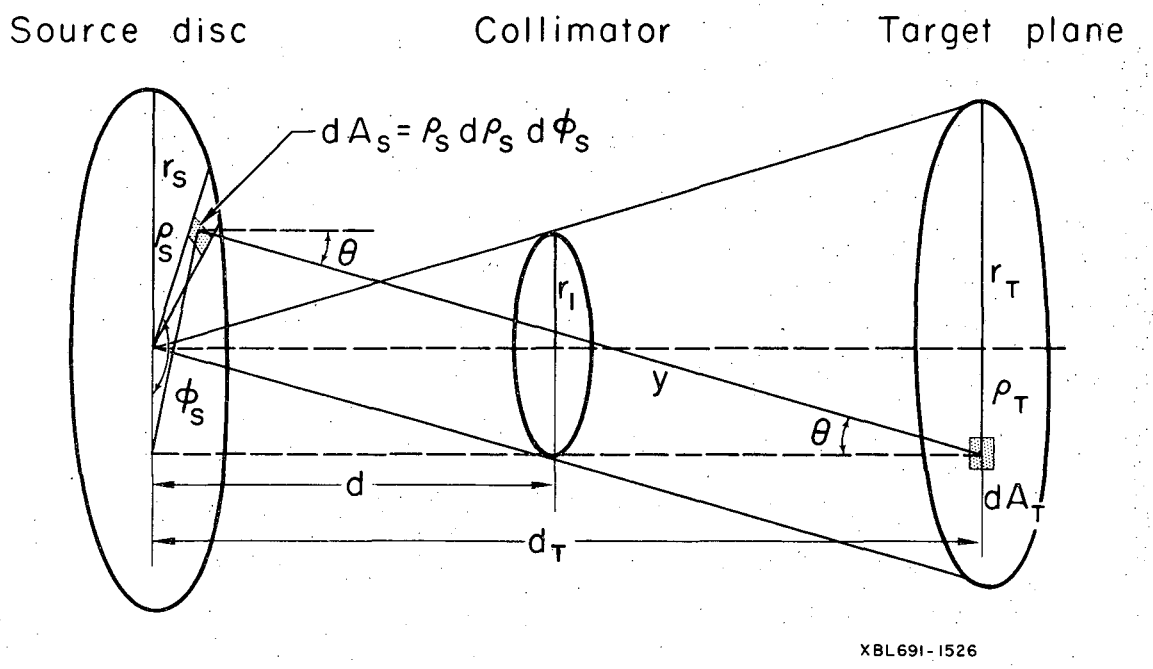

Fig. 2 Diagram for calculating molecular beam intensities from non-point sources.

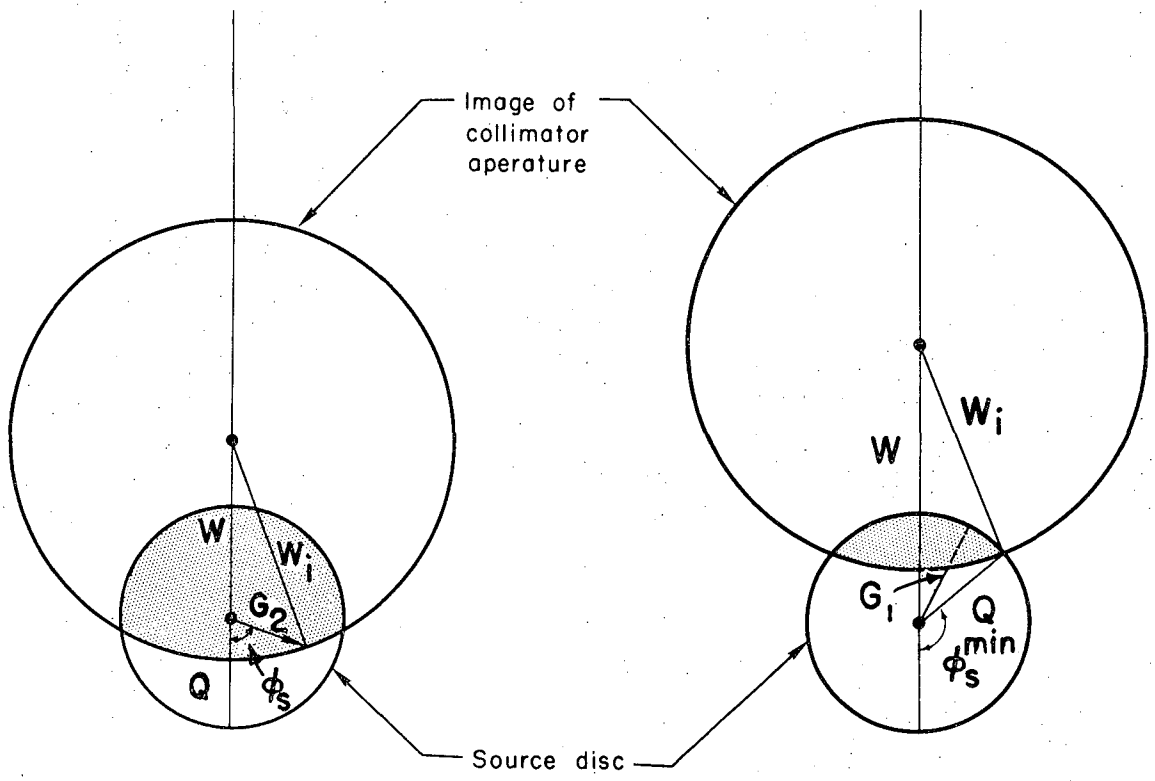

(a) $W_i > W$

(b) $W_i < W$

XBL 691-1517

Fig. 3 Region of overlap between source disk and the image of the collimating aperture projected on the source plane from an off-axis location on the target.

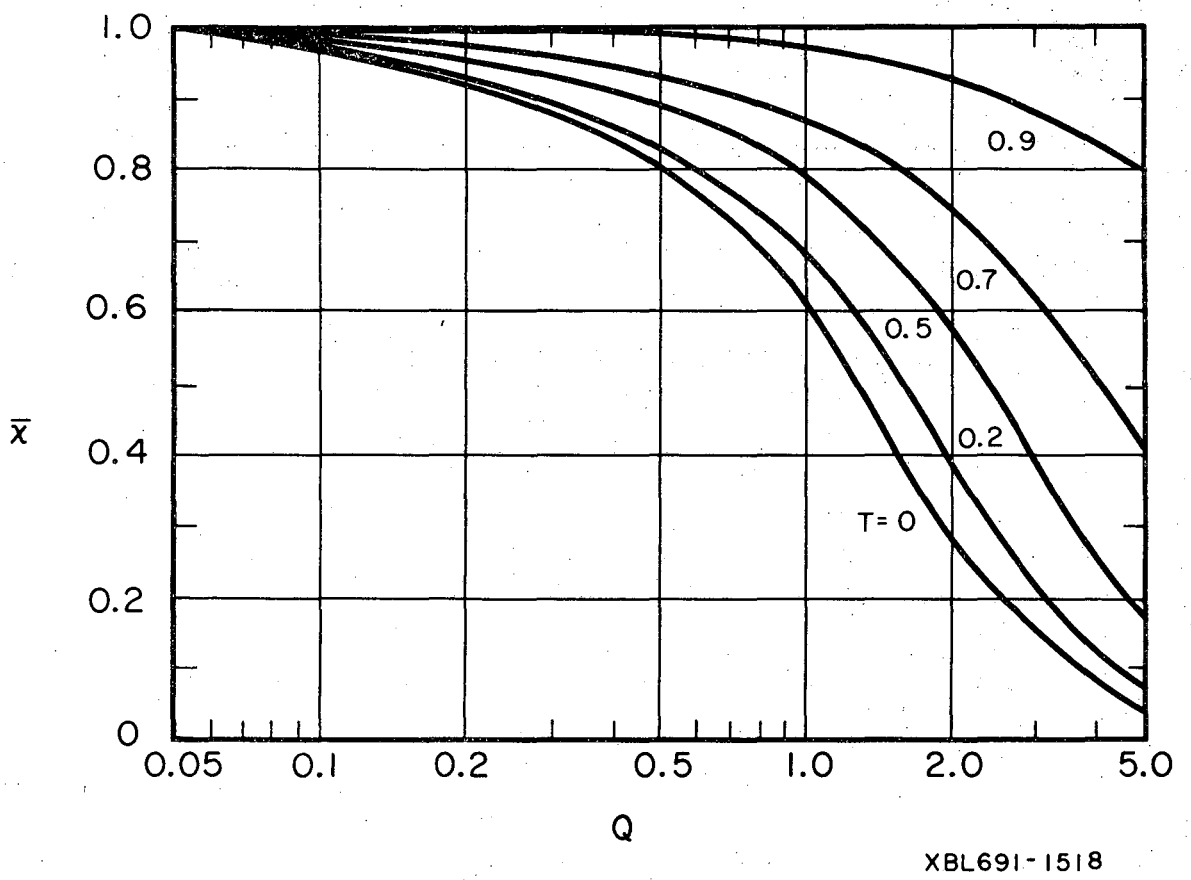

Fig. 4 Average peaking factor (or the ratio of usable beam fluxes) for non-point cosine sources as a function of the ratios $T = d/d_T$ and $Q = r_s/r_l$.

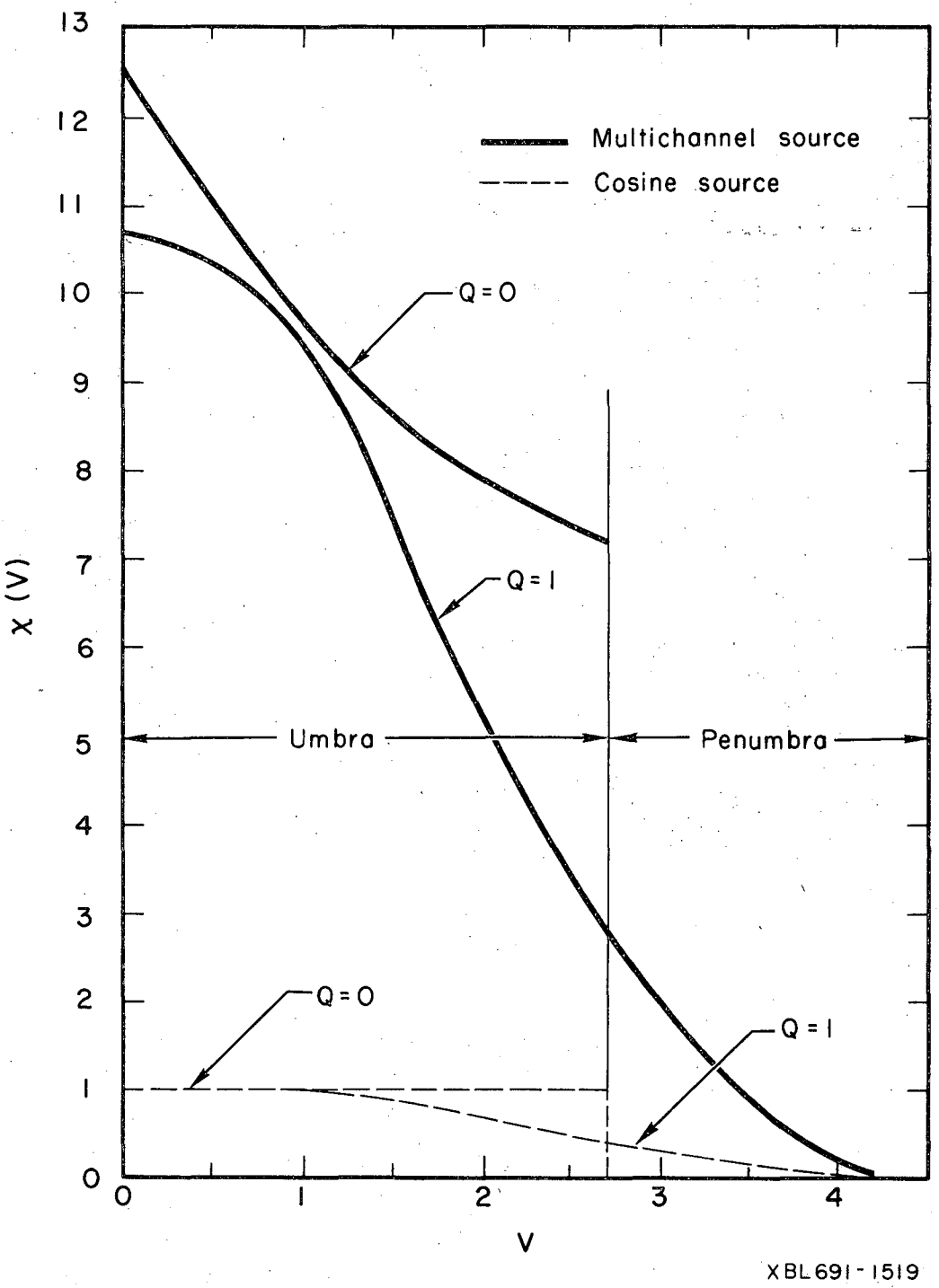

Fig. 5 Beam intensities on the target from point and finite sources for R = 0.044 and T = 0.37.

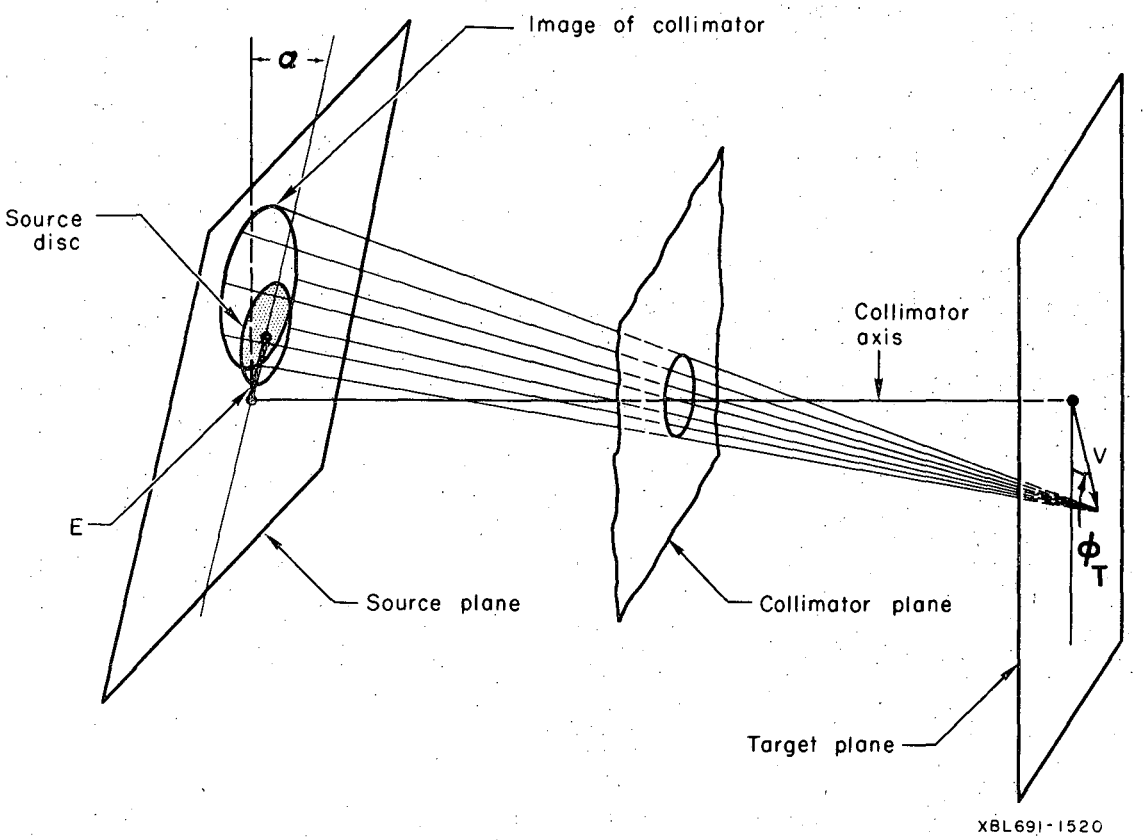

Fig. 6 Beam geometry with displacement and tilt misalignment.

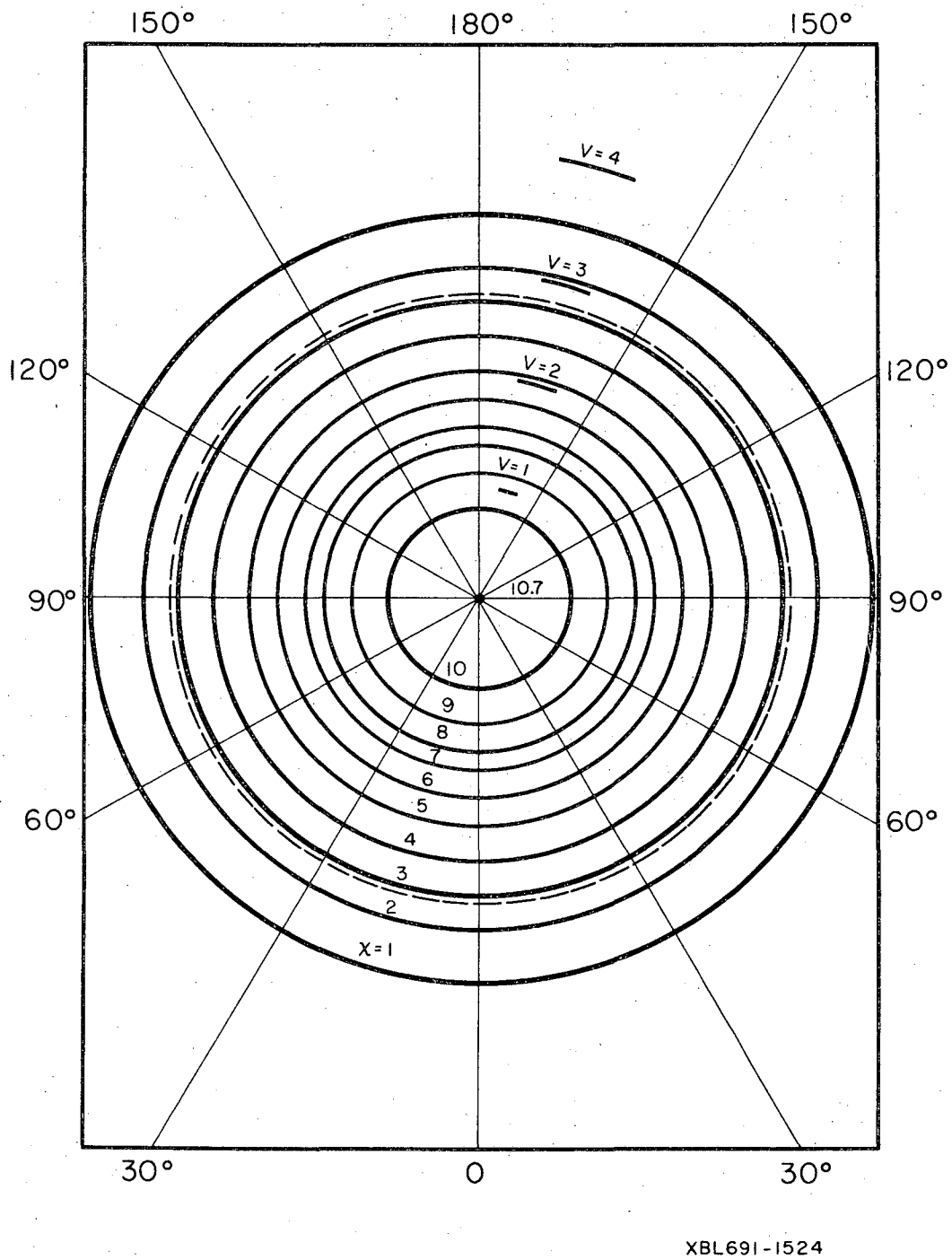

Fig. 7 Beam intensity contours on target from perfectly aligned multichannel source. Q = 1, R = 0.044, T = 0.37.

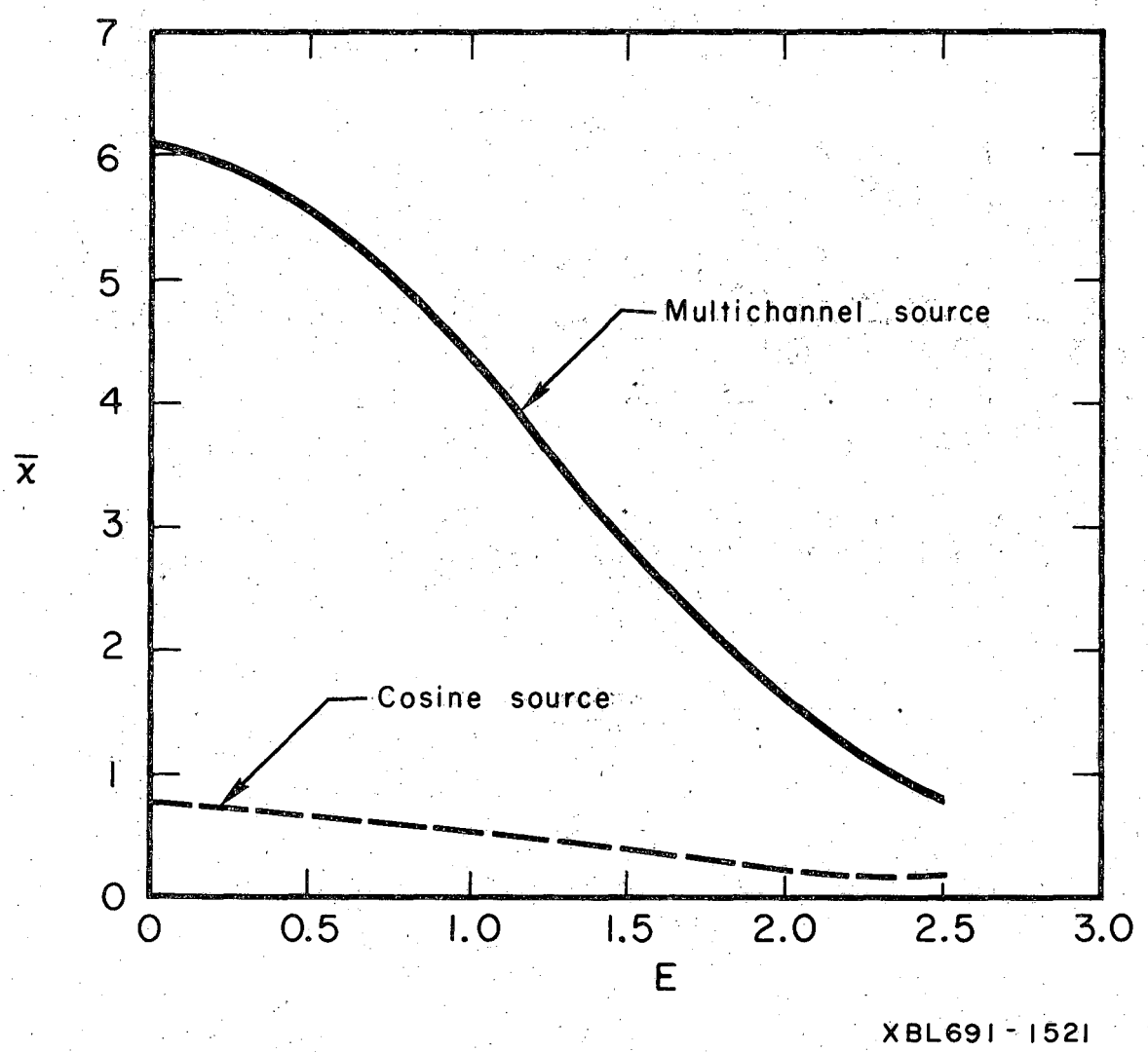

Fig. 10 Effect of displacement on average peaking factor from multichannel source. Q = 1, R = 0.044, T = 0.37, α = 0.

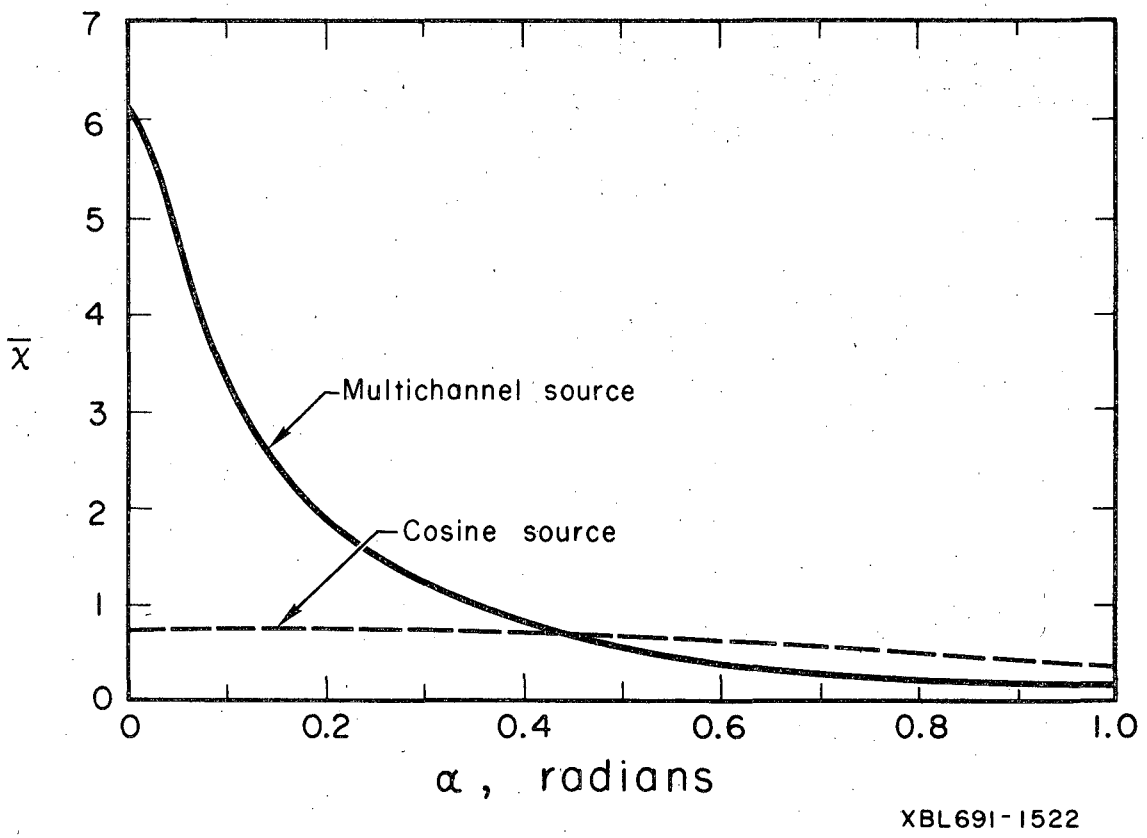

Fig. 11 Effect of tilt on average peaking factor from multichannel source. Q = 1, R = 0.044, T = 0.37, E = 0.

LEGAL NOTICE

TECHNICAL INFORMATION DIVISION
LAWRENCE RADIATION LABORATORY
UNIVERSITY OF CALIFORNIA
BERKELEY, CALIFORNIA 94720